energies

MDPI

Article

RBF Neural Network-Based Sliding Mode Control for Modular Multilevel Converter with Uncertainty Mathematical Model

Xuhong Yang and Haoxu Fang *

College of Automation Engineering, Shanghai University of Electric Power, Shanghai 200090, China; yangxuhong.sh@163.com

* Correspondence: fanghaoxu@163.com or fanghaoxu@mail.shiep.edu.cn

Abstract: For medium and high-powered applications, modular multilevel converters have become the most promising converter application. In this paper, a sliding mode controller based on an RBF neural network is proposed for a modular multilevel converter. The RBF neural network is designed to approximate the uncertainty mathematical model of a modular multilevel converter. The main innovation of the proposed method is that it does not require any model parameters and control parameters during the whole control process. This means that parameter changes caused by the external environment will not influence the controller performances. Finally, by comparing with a conventional PI controller, the simulation proves the feasibility and effectiveness of the proposed control method. In addition, the experimental results show that the grid-side current can become stable immediately while the active power is stabilized after 20 ms when the set value is changed.

Keywords: modular multilevel converter; sliding mode control; RBF neural network; uncertainty mathematical model

Citation: Yang, X.; Fang, H. RBF Neural Network-Based Sliding Mode Control for Modular Multilevel Converter with Uncertainty Mathematical Model. *Energies* **2022**, *15*, 1634. https://doi.org/10.3390/en15051634

Academic Editor: Alon Kuperman

Received: 24 January 2022
Accepted: 16 February 2022
Published: 22 February 2022

1. Introduction

With the development of power electronic devices, DC transmission devices have also changed from two-level converters to three-level converters and finally to modular multilevel converters (MMC).

However, the intricated structure of the MMC makes it difficult to control and analyze effectively [1,2]. In order to improve its operating performance, extensive research has been conducted in recent years to address the technical challenges and MMC operation and control [3,4]. For this purpose, conventional proportional-integral controllers (PI) [5] and proportional-resonant (PR) control [6] have been proposed based on classical control theory and the mathematical model of the MMC. Although the classical controller can control the internal dynamics of the MMC, due to the strong nonlinearity of the MMC and the complex coupling, it is necessary to use nonlinear control techniques to obtain a better output [7–11]. Then, various nonlinear control techniques, such as sliding mode control [7], Lagrange multiplier-based optimal control [8], model-based input–output linearization [9], and developed feedback linearization [10], have also been proposed and researched. Another control approach is model predictive control [12–14]. It was originally proposed by Richalet and Cutleris and now is widely used in power electronics. However, the main drawback of MPC is the high performance of the computer. When applied in MMC, the GPU frequency required is higher due to the larger number of sub-modules. That is, the MPC algorithm should be able to evaluate all possible capacitor voltage combinations within one sample period. In other words, higher GPU will also increase the cost. In addition, conventional nonlinear controller-based techniques rely on a precise mathematical model of the system, which is difficult to achieve in real life.

Furthermore, there are frequently unknown nonlinear functions in nonlinear systems. Because of its universal approximation of any unknown smooth nonlinear function, the neural network (NN) is commonly utilized in nonlinear systems. Ref. [15] used NN

to approximate the nonlinear part in the APF. Ref. [16] also introduces the same idea. Refs. [17–19] used NN to approximate the mathematical model of MMC and then control using MPC. However, the MPC and NN have increased the cost and the burden on the computer.

Power electronic converters are variable structure systems due to the switching devices. Therefore, the sliding mode controller (SMC) is suitable for power electronic converters as a variable structure controller. SMC were first proposed in 1950 [20,21]. SMC is a nonlinear control method. It is suitable for the control of power converters and can achieve better regulation and dynamic performance over a wider range of operating conditions. The main reason is that the nonlinear controller design does not require a linear model of the power converter. Sliding mode controllers are widely used in DC-DC converters. Mazumder et al. firstly proposed an integral variable structure sliding mode controlled parallel buck converter based on a fixed frequency PWM [22]. This technique was later extended to the application of controlled voltage regulation modules [23]. Later, a unified PWM-based fixed-frequency direct sliding mode voltage control design scheme was proposed for buck, boost, and buck–boost converters [24]. However, the sliding mode controller has the problem of jitter, which will reduce stability [25]. Therefore, if the sliding mode controller is applied to AC-DC, it will increase the harmonics of the grid current and the output power will be jittered. In this paper, NN solves the jitter problem of sliding mode control by fitting the sliding mode control law.

RBFSMC was first proposed in 2006 [26]. The RBF is used to adjust the controller parameters of the SMC or to fit the nonlinear part of the controlled object. Nowadays, RBFSMC is mainly used in Ship's Heading [27], robotics [28,29], and aeronautical remote sensing stable platforms [30]. Motivated by the above studies, a sliding-mode controller using the RBF neural network (RBFNN) structure is proposed for the current control of MMC. In this paper, RBF is mainly used to fit the SMC control law. The main advantages of using an RBF neural network-based sliding mode control in this paper are as follows: (i) no device parameters are required; (ii) no controller parameters are required; (iii) no jitter; (iv) stable operation when the grid voltage drops; (v) suitable for all MMC systems. Finally, simulation and experimental results verify the effectiveness of RBFSMC.

2. Mathematical Model of MMC

The topology of three phases MMC is shown in Figure 1. Three phase MMC mainly consist of an upper and a lower arm as well as two small coupling inductances. Each arm has the same number of sub-modules (SMs). The SM consists of two IGBT half bridges with anti-parallel diodes and one parallel capacitor.

In Figure 1, making use of Kirchhoff's law, the mathematical model of MMC can be obtained:

$$\begin{cases} u_{sa} = u_a - L_0(di_{sa}/dt) - R_0 i_{sa} \\ u_{sb} = u_b - L_0(di_{sb}/dt) - R_0 i_{sb} \\ u_{sc} = u_c - L_0(di_{sc}/dt) - R_0 i_{sc} \end{cases} \tag{1}$$

$$u_{dc} = u_{mp} + u_{jn} + 2L_i \frac{di_{cirj}}{dt} \tag{2}$$

In addition, the port voltages of upper arm and lower arm can be expressed as

$$\begin{cases} u_{ip} = u_{dc}/2 - u_i - u_{cirj} \\ u_{in} = u_{dc}/2 + u_i - u_{cirj} \end{cases} \tag{3}$$

Transforming Equation (1) into dq coordinate, we can obtain:

$$\begin{cases} u_d = u_{sd} + \omega L_0 i_{sq} - R_0 i_{sd} - L_0 \frac{\mathrm{d}i_{sd}}{\mathrm{d}t} \\ u_q = u_{sq} + \omega L_0 i_{sd} - R_0 i_{sq} - L_0 \frac{\mathrm{d}i_{sq}}{\mathrm{d}t} \end{cases} \tag{4}$$

where, u_{sm}/i_{sm} represent three-phase output voltages/currents; u_m represent three-phase AC voltages on the converter side; R_0 and L_0 are the line resistance and inductance; u_{jP} and u_{jN} are the port voltages of the upper arm and lower arm; i_{cirj} is the circulation current; u_{cirj} is the voltage drop caused by i_{cirj}; L_i is the inductance of the bridge arm; u_{dc} is the DC voltage; m = a, b, c, d, q. i = a, b, c.

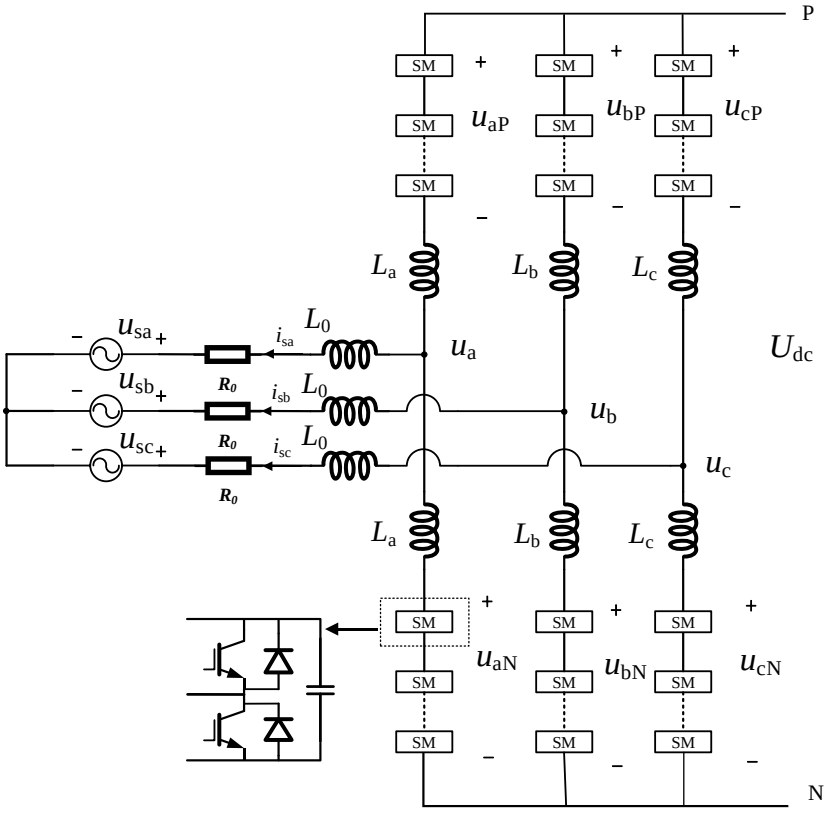

Figure 1. Topology of the MMC.

By defining $x_1 = i_{sd}$, $x_2 = i_{sq}$, Equation (4) can be transformed as

$$\begin{gathered} \begin{cases} \dot{x}_1 = f_1(x_1, x_2) + bu_d \\ \dot{x}_2 = f_2(x_1, x_2) + bu_q \end{cases} \\ f_1(x_1, x_2) = \frac{u_{sd}}{L_0} + \omega x_2 - \frac{R_0}{L_0} x_1 \\ f_2(x_1, x_2) = \frac{u_{sq}}{L_0} + \omega x_1 - \frac{R_0}{L_0} x_2 \end{gathered} \tag{5}$$

3. Control Strategy Design

3.1. Design of PI Controller

According to Equation (4), the PI controller can be designed as

$$\begin{cases} u_d = K_p\left(i_{sdref} - i_{sd}\right) + K_i \int \left(i_{sdref} - i_{sd}\right)dt + \omega L_o i_{sq} + u_{sd} \\ u_q = K_p\left(i_{sqref} - i_{sq}\right) + K_i \int \left(i_{sqref} - i_{sq}\right)dt - \omega L_o i_{sd} + u_{sq} \end{cases} \tag{6}$$

Applying the Laplace transform theory, the open-loop transfer function of the current loop is obtained

$$\begin{gathered} G(s) = \frac{K_i(\tau_i s+1)}{s(1.5T_s s+1)(R_0+sL_0)} \\ \tau_i = \frac{K_p}{K_i} \end{gathered} \tag{7}$$

where, K_p and K_i are the controller parameters and T_s is the switching times.

Applying the M_r minimum criterion method, letting $\frac{\tau_i}{1.5T_s} = 1$, the closed-loop transfer function of the current loop is obtained

$$G_1(s) = \frac{\frac{K_i}{L}}{s^2 + \frac{R}{L}s + \frac{K_i}{L}} \tag{8}$$

According to the 2nd order system theory, we obtain the range of PI controller parameters

$$\begin{cases} 0 < \varepsilon = \frac{R_0}{2\omega_n L_0} < 1 \omega_n = \sqrt{\frac{K_i}{L_0}} \\ K_p > 0 \end{cases} \tag{9}$$

3.2. Design of Sliding Mode Controller

The goal of the SMC is to ensure high dynamic tracking performance. According to the SMC theory, the sliding mode surface is designed as

$$\begin{cases} s_1 = x_1 - x_{1ref} = i_{sd} - i_{sdref} \\ s_2 = x_2 - x_{2ref} = i_{sq} - i_{sqref} \end{cases} \tag{10}$$

where, i_{sqref} is the reference current of the q-axis and i_{sdref} is the reference current of the d-axis.

In fact, in power electronic systems, the d-axis reflects active power and the q-axis reflects reactive power. Therefore, the reference current can be given by Equation (11)

$$\begin{cases} i_{dref} = \frac{2}{3} \times \frac{P_{ref}}{u_{sd}} \\ i_{qref} = -\frac{2}{3} \times \frac{Q_{ref}}{u_{sd}} \end{cases} \tag{11}$$

where, P_{ref} and Q_{ref} are the setting values of active and reactive power.

To compensate for the effect of the lumped uncertainties, we design the exponential reaching law as follows

$$\begin{cases} \dot{s}_1 = -\varepsilon_1 \mathrm{sgn}(s_1) - q_1 s_1 \\ \dot{s}_2 = -\varepsilon_2 \mathrm{sgn}(s_2) - q_2 s_2 \end{cases} \tag{12}$$

where, ε and q are positive constants.

With derivative Equation (10) and combined with Equation (12), we can obtain

$$\begin{cases} u_d = -\frac{1}{b} \times (f_1(x_1, x_2) + \varepsilon_1 \mathrm{sgn}(s_1) + q_1 s_1) \\ u_q = -\frac{1}{b} \times (f_2(x_1, x_2) + \varepsilon_2 \mathrm{sgn}(s_2) + q_2 s_2) \end{cases} \tag{13}$$

In order to reduce the high frequency jitter of the SMC, the saturation function sat$(\cdot)$ is used instead of the sign function sgn$(\cdot)$ in the ideal sliding mode, and Equation (13) can be transformed as

$$\begin{cases} u_d = -\frac{1}{b} \times (f_1(x_1, x_2) + \varepsilon_1 sat(s_1) + q_1 s_1) \\ \quad = -\frac{1}{b} \times F_1(x_2, s_1) \\ u_q = -\frac{1}{b} \times (f_2(x_1, x_2) + \varepsilon_2 sat(s_2) + q_2 s_2) \\ \quad = -\frac{1}{b} \times F_2(x_1, s_2) \end{cases} \tag{14}$$

In addition, under unbalanced grid voltage, Equation (14) can be transformed in positive and negative orders

$$\begin{cases} u_d^+ = -\frac{1}{b} \times (f_1^+(x_1^+, x_2^+) + \varepsilon_1 sat(s_1) + q_1 s_1) \\ \quad = -\frac{1}{b} \times F_1^+(x_2^+, s_1) \\ u_q^+ = -\frac{1}{b} \times (f_2^+(x_1^+, x_2^+) + \varepsilon_2 sat(s_2) + q_2 s_2) \\ \quad = -\frac{1}{b} \times F_2^+(x_1^+, s_2) \end{cases} \tag{15}$$

$$\begin{cases} u_d^- = -\frac{1}{b} \times (f_1^-(x_1^-, x_2^-) + \varepsilon_3 sat(s_3) + q_3 s_3) \\ \quad = -\frac{1}{b} \times F_1^-(x_2^-, s_3) \\ u_q^- = -\frac{1}{b} \times (f_2^-(x_1^-, x_2^-) + \varepsilon_4 sat(s_4) + q_4 s_4) \\ \quad = -\frac{1}{b} \times F_2^-(x_2^-, s_4) \end{cases} \tag{16}$$

3.3. Stability Analysis

To prove convergence and stability of the proposed SMC, the matrix **S** is defined as

$$\mathbf{S} = \begin{bmatrix} s(t) & 0 \end{bmatrix} \tag{17}$$

Consider the following positive definite Lyapunov candidate function

$$\mathrm{V} = \mathbf{S}\mathbf{S}^{\mathrm{T}} = [s(t)]^2 \tag{18}$$

Taking the derivative of Equation (18), and combining Equation (12) results in

$$\dot{\mathrm{V}} = 2s(-\varepsilon sat(s) - qs) = -\left(\varepsilon \left| s \right| + qs^2\right) \tag{19}$$

Because the controller parameters ε and q are positive, we can find $\mathrm{V} > 0$ and $\dot{\mathrm{V}} < 0$. In other words, the controlled system satisfies the reaching condition.

Practically, MMC is constantly influenced by a variety of unknown disturbances and parametric variations caused by aging inductors and capacitors, which must be accounted for in the system model. However, the parametric variations caused by aging inductors and capacitors is a nonlinear function. As $f_1(x_1, x_2)$ and $f_2(x_1, x_2)$ in Equation (14) are unknown, it is impossible to implement the control law Equation (14). In addition, the ε and q will also affect the stability of the controller, which should be considered. RBFNN can fit arbitrary nonlinear functions due to its specific neuron structure. RBFNN was used to fit Equation (14) in this paper.

4. RBF Neural Network-Based Sliding Mode Control

4.1. Design of RBF NN

The input layer, hidden layer, and output layer are the basic three layers of forward structure in RBF NN. Basic RBF NN is shown in Figure 2.

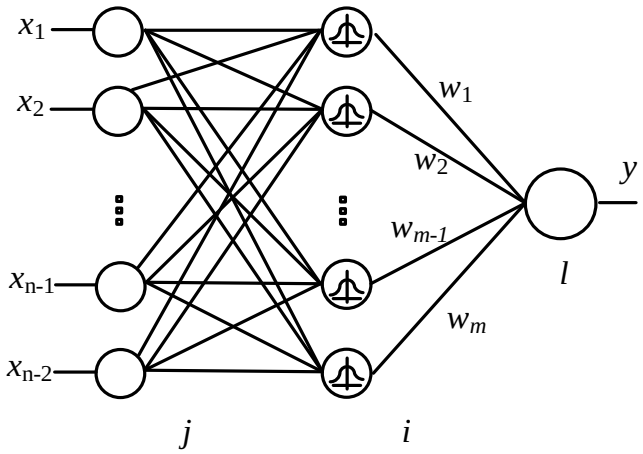

Figure 2. Basic RBF NN.

It can be seen in Figure 2 that the input of RBF NN is Equation (20)

$$\mathrm{x} = \left[x_1, x_2, \ldots x_j\right]^{\mathrm{T}}, j = 1, 2, \ldots, n \tag{20}$$

The output of each neuron in the middle layer is Equation (21)

$$h_i = \exp\left(-\frac{\|\boldsymbol{x} - \boldsymbol{a}_i\|^2}{2\boldsymbol{b}_i^2}\right), i = 1, 2, \ldots, m \tag{21}$$

where, $\boldsymbol{a}_i = [a_{i1}, \ldots, a_{in}]$ is the center vector of the i-th hidden layer neuron. The width vector of Gauss function is $\boldsymbol{b}_i = [b_1, b_2, \ldots, b_m]^{\mathrm{T}}$.

According to the rules of neural network calculation, the output is Equation (22)

$$y = \boldsymbol{w}^T \boldsymbol{h} \tag{22}$$

where, $\boldsymbol{\omega}^{\mathrm{T}}$ is the weight of NN, $\boldsymbol{h}_i = [h_1, h_2, \ldots, h_m]^{\mathrm{T}}$.

(1) *Number of neurons:* When the control system is confirmed, the number of input and output neurons is also determined. In this paper, the input values of the d-axis are x_2 and s_1 and the q-axis are x_1 and s_2, so the number of input neurons of d-axis and q-axis nodes is 2. The output variable of the d-axis is u_d and the variable of the q-axis is u_q. There is no currently uniform formula to determine the number of middle layer neurons. According to simulation results, the best results are obtained when the number of neurons in the middle layer is 8. The input and output layers are 2 and 1, respectively.

(2) *Parameter Setting*: The settings of $\boldsymbol{a}_{\mathrm{i}}$ and $\boldsymbol{b}_{\mathrm{i}}$ also affect the output of RBFNN. When the input is close to $\boldsymbol{a}_{\mathrm{i}}$, the value of Gauss function is sensitive and $\boldsymbol{b}_{\mathrm{i}}$ is the mapping range of the Gauss function. In this paper, $\boldsymbol{a}_{\mathrm{i}}$ is 0 and $\boldsymbol{b}_{\mathrm{i}}$ is 1.

4.2. RBF NN Sliding Mode Controller

The RBFNN is used to approximate the nonlinear functions $F_1(x_2, s_1)$ and $F_2(x_1, s_2)$. Take $F_1(x_2, s_1)$ as an example. The RBF neural network-based sliding mode control (RBFSMC) block diagram of the d-axis (q-axis) is shown in Figure 3.

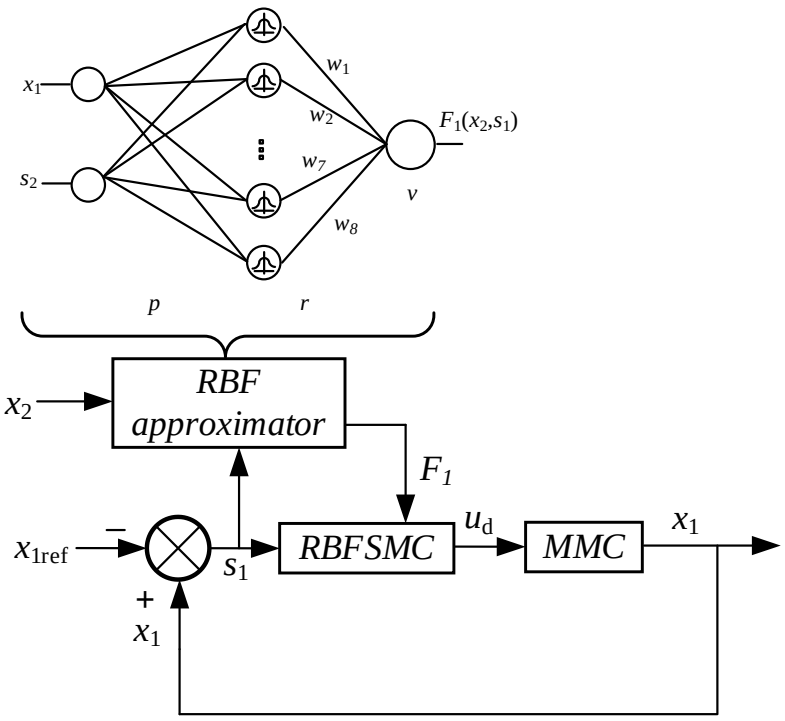

Figure 3. The RBFSMC control block diagram of the d-axis (q-axis).

The input of RBFSMC shown in Figure 3 is

$$O_p^{(1)} = x(p), p = 1, 2, \tag{23}$$

where, $x(1) = x_2$, $x(2) = s_1$;

The input of the hidden layer is

$$\text{net}_r^{(2)} = \boldsymbol{x}, \boldsymbol{x} = (x(1), x(2)) \tag{24}$$

The output of the hidden layer is

$$O_r^{(2)}(k) = g\left(\text{net}_r^{(2)}(k)\right), r = 1, 2 \ldots 8 \tag{25}$$

To distinguish across layers, superscripts (1)–(3) are used to denote input, hidden, and output layers, respectively. The Gauss function is $g(x)$.

The input of RBFSMC's output layer is

$$\text{net}_r^{(3)}(k) = \sum_{r=1}^{8} w_{lr}^{(3)} O_r^{(2)}(k) \tag{26}$$

Finally, the output of RBFSMC is F_1:

$$F_1 = O_r^{(3)}(k) = f\left(\text{net}_v^{(3)}(k)\right), v = 1 \tag{27}$$

5. Simulation Results

To show the validity of the suggested controller, we built the model in MATLAB/Simulink according to Figures 1 and 4. The system parameters and controller parameters are listed in Tables 1 and 2.

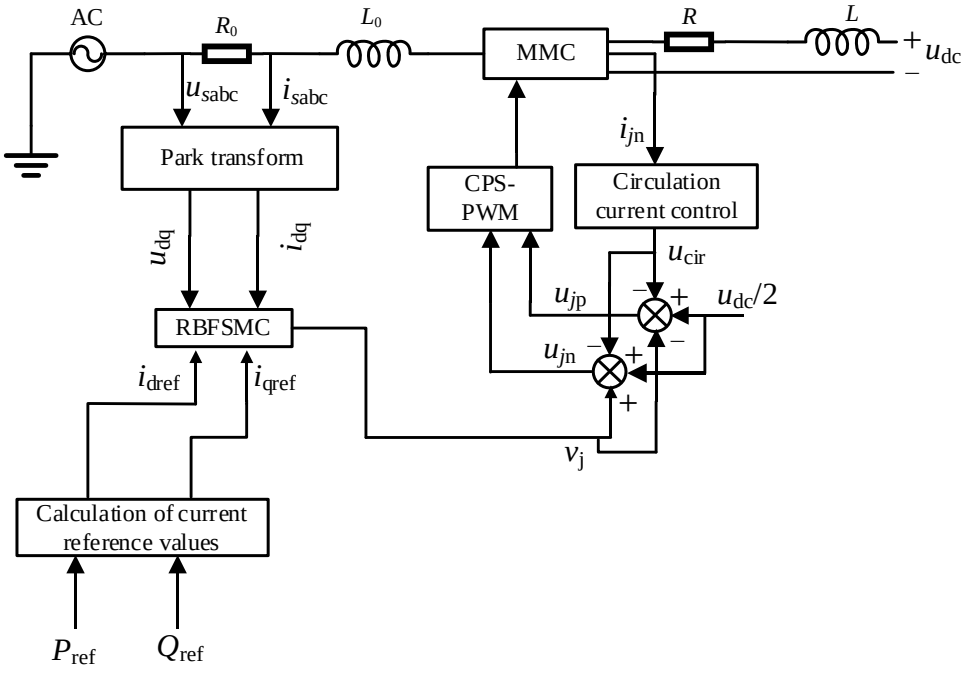

Figure 4. The block diagram of the MMC control system.

5.1. Steady-State Performance

Figure 5 shows the three-phase grid-side current of MMC. As can be seen in Figure 5, the grid-side current has almost no setting time to become stable using the controller proposed in the paper. To determine the harmonic content of the grid-side currents, fast Fourier transforms (FFT) of Phase A of the grid-side current are shown in Figure 6. From Figure 6, the FFT of the grid-side current have good performance under RBFSMC.

Table 1. Simulation experiment parameters.

System Parameter	Value
Grid voltage	20 kV
DC voltage	20 kV
Filter inductors	5 mH
Line equivalent resistance	0.047 Ω
Number of single bridge arm sub-modules	10
Arm inductance	5 mH
Active power	7 MW (9 MW)
Reactive power	0 Var
Switching frequency	2 KHz

Table 2. Controller parameters.

Controller Parameter	Value
Number of neurons in the middle layer	8
Number of neurons in the input layer	2
Number of neurons in the output layer	1
a_i,b_i	0.1
K_p	5
K_i	0.5

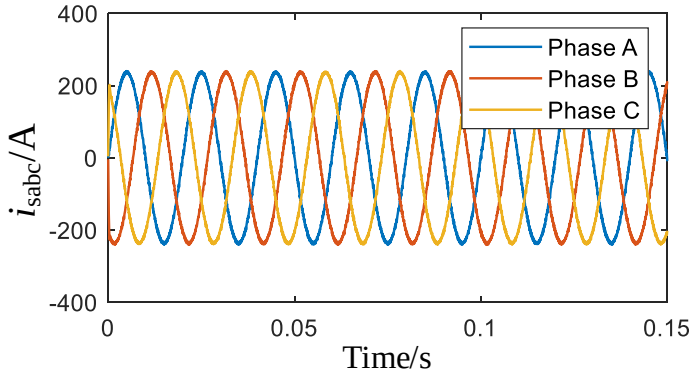

Figure 5. Grid-side current.

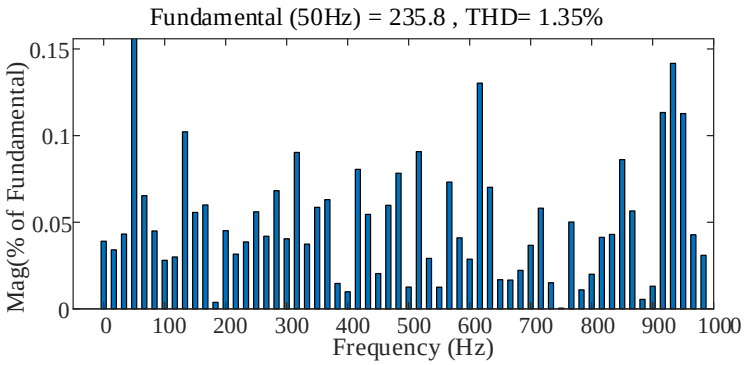

Figure 6. FFT analysis of the grid-side current.

Figure 7 shows the circulating current of Phase A. As can be seen in Figure 7, the circulating current is suppressed after 0.005 s and the peak value is 35 A at 0.002 s. Submodule capacitance voltage is a key parameter in the MMC. The submodule capacitance voltage of A phase is shown in Figure 8. The submodule capacitance voltage is stable at 4000 V and varies in the same trend. The results illustrate that the RBFSMC can work well with traditional capacitor voltage control as well as the loop current suppression.

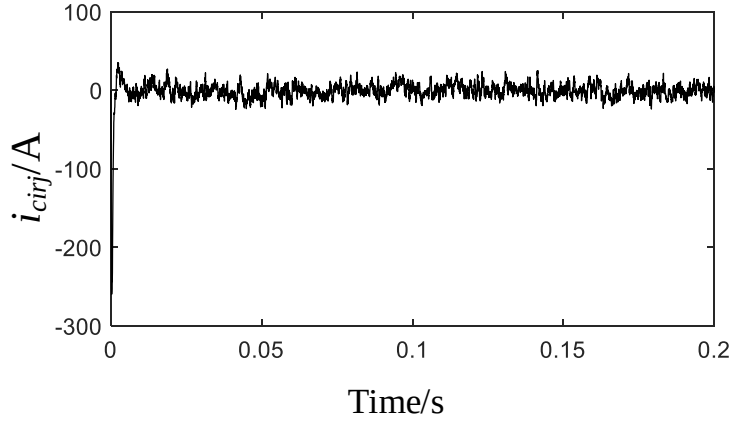

Figure 7. Circulating current of Phase A.

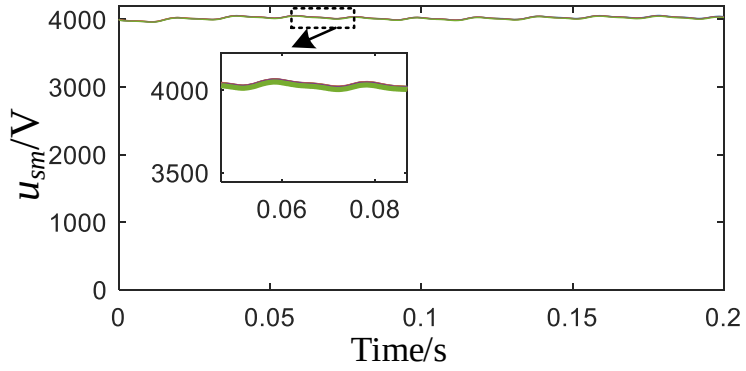

Figure 8. Waveforms of submodule capacitance voltage.

Figure 9 shows the active and reactive power of MMC under RBFSMC. It can be seen from Figure 9 that the active and reactive power can be stable. The overshoot of the active power is 4.7% and the setting time is 0.03s. The reactive power is constant without fluctuations in operation

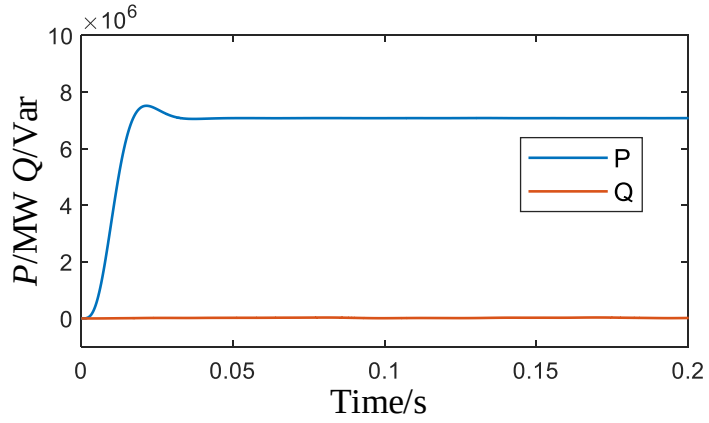

Figure 9. Waveforms of active and reactive power.

Figure 10 shows the *d*-axis and *q*-axis components of grid currents. In Figure 10a,b, the d-axis component and *q*-axis component can track the reference values quickly without delay. The results show that the dynamic performance and tracking performance is good under RBFSMC.

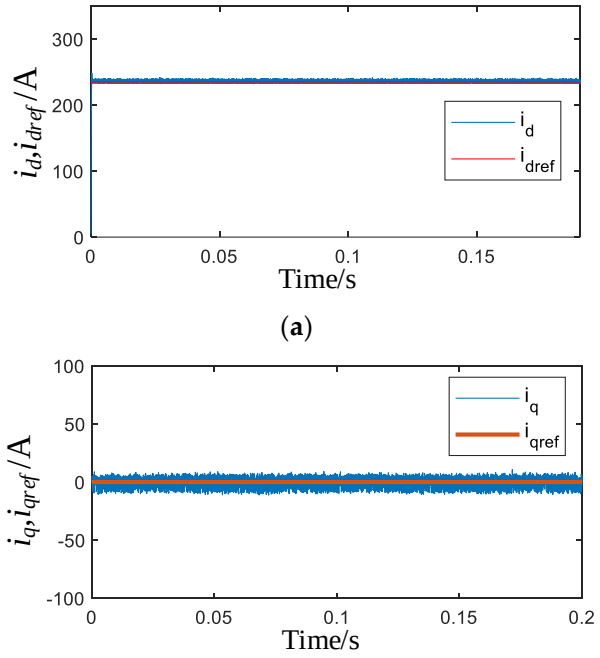

Figure 10. The response of *d*-axis and *q*-axis components: (**a**) *d*-axis component; (**b**) *q*-axis component.

In addition, to verify that RBFSMC is not affected by grid voltage, the grid voltage was changed to 18 kV (grid voltage drops 10%). Figure 11 shows the grid-side current and power when the grid voltage is 18 kV. As can be seen in Figure 11, the current and power can still become stable quickly. That means the changes in grid voltage have little effect on the current and power.

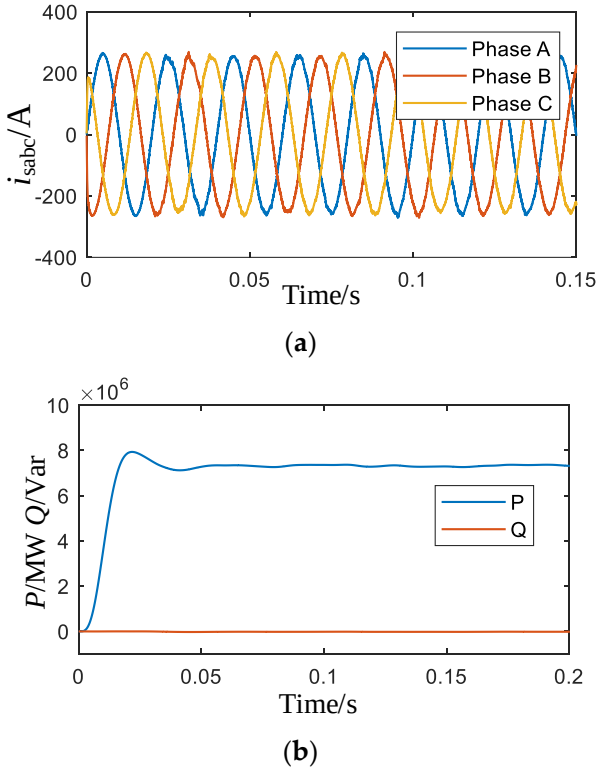

Figure 11. Waveforms of current and power: (**a**) grid-side current; (**b**) power.

5.2. Dynamic Performance

To verify the speed and effectiveness of controller, the active power increases abruptly from 7 to 9 MW at 0.2 s in this paper and compared with conventional PI control. Figure 12 shows waveforms of the grid-side current from 0.18 to 0.23 s. Simulation result analysis of grid-side current is shown in Table 3. As can be seen in Figure 12, the amplitude of the grid current is larger when the active power reference changes. The grid current fluctuates when the set value changes and it takes about 1 ms to become stable. However, PI control needs 10 ms and the waveforms are worse than RBFSMC.

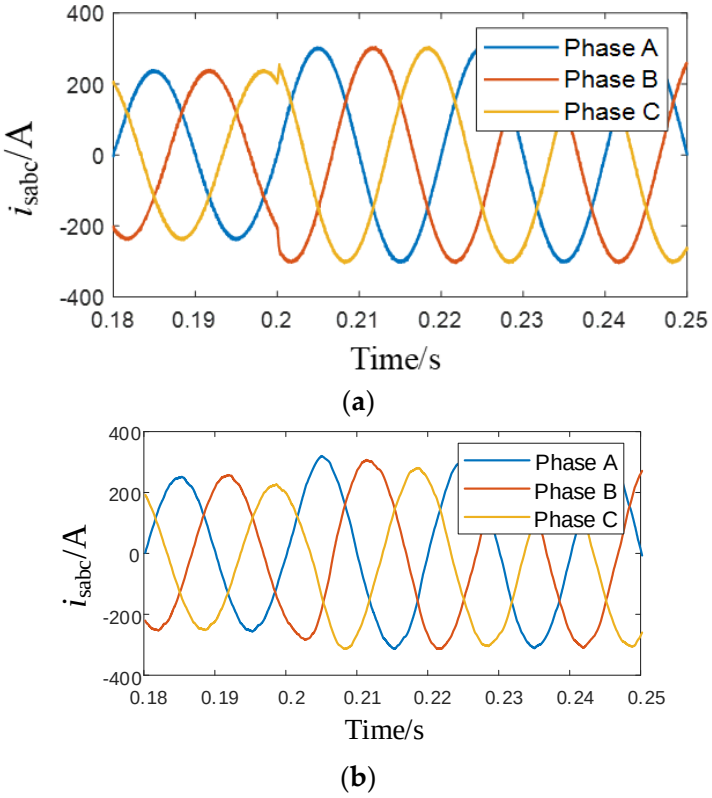

Figure 12. Grid-side current under active power changes: (**a**) RBFSMC; (**b**) PI control.

Table 3. Simulation result analysis of grid-side current.

Grid-Side Current	Dynamic Response Time	FFT
RBFSMC	1 ms	1.35%
PI control	10 ms	1.7%

Figure 13 shows waveforms of the *d*-axis and *q*-axis current under active power changes. In Figure 13a, because of the set value changes, i_{dref} will change from 235 to 300 A. The i_d under RBFSMC can track the signal immediately at 0.2 s without any fluctuation and overshoot. However, the i_d under PI control has a big overshoot when MMC starts and takes about 10 ms to become stable after 0.2 s. In addition, it can be seen in Figure 13b that the value of i_{qref} is 0 and there is no fluctuation at 0.2 s under RBFSMC. From Table 4, we find that the result is better than PI control.

Figure 14 shows waveforms of active and reactive power of MMC. Simulation result analysis of power is shown in Table 5. It can be seen in Figure 14 that the peak value of active value is 9.098 MW and the setting time is 0.02 s when the active power changes. The reactive power is still constant with no fluctuation at 0.2 s. The results show that RBFSMC proposed in this paper has good dynamic performance and faster response than PI control.

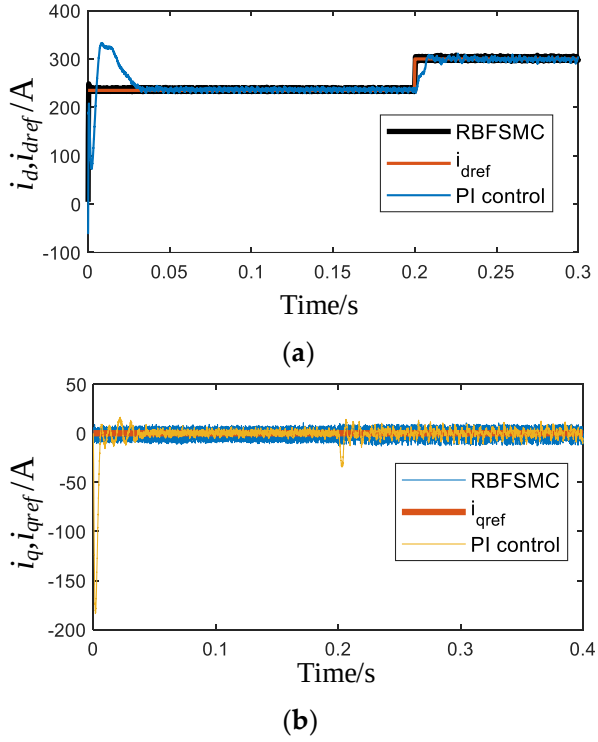

Figure 13. The response of *d*-axis and *q*-axis components under RBFSMC and PI control: (**a**) *d*-axis component; (**b**) *q*-axis component.

Table 4. Simulation result analysis of *dq* current.

d-Axis and *q*-Axis Current		Maximum Inrush Current	Dynamic Response Time
RBFSMC	*d*-axis current (i_d)	245 A	0.5 ms (started), 1 ms (changed)
	q-axis current (i_q)	3.5 A	0 ms (started), 0 ms (changed)
PI control	*d*-axis current (i_d)	330 A	30 ms (started), 20 ms (changed)
	q-axis current (i_q)	182 A	30 ms (started), 20 ms (changed)

5.3. Unbalanced Grid Voltage Performance

In this paper, the voltage of phase A dropped by 10% (20 kV→18 kV), while phase B and phase C maintained the original voltage. Because of the unbalanced grid voltage, it is found that the instantaneous power of MMC is changed as follows:

$$\begin{bmatrix} P_{s0} \\ P_{s2\sin} \\ P_{s2\cos} \\ Q_{s0} \\ Q_{s2\sin} \\ Q_{s2\cos} \end{bmatrix} = \frac{3}{2} \begin{bmatrix} u_{sd}^{+} & u_{sq}^{+} & u_{sd}^{-} & u_{sq}^{-} \\ u_{sq}^{-} & -u_{sd}^{-} & -u_{sq}^{+} & u_{sd}^{+} \\ u_{sd}^{-} & u_{sq}^{-} & u_{sd}^{+} & u_{sq}^{+} \\ u_{sq}^{+} & -u_{sd}^{+} & u_{sq}^{-} & -u_{sd}^{-} \\ -u_{sd}^{-} & -u_{sq}^{+} & u_{sd}^{+} & u_{sq}^{+} \\ u_{sq}^{-} & -u_{sd}^{-} & u_{sd}^{+} & u_{sq}^{+} \end{bmatrix} \begin{bmatrix} i_{sd}^{+} \\ i_{sq}^{+} \\ i_{sd}^{-} \\ i_{sq} \end{bmatrix} \tag{28}$$

where, u_{sn}^{m} is the positive and negative sequence components of the output voltage on the AC side in the d/q axis, respectively; i_{sn}^{m} is the positive and negative sequence components of the output current on the AC side in the d/q axis, respectively; $P(Q)_{s0}$, $P(Q)_{s2\sin}$, $P(Q)_{s2\cos}$ are the direct flow of active (reactive) power, the two sine components of the secondary fluctuation, and the cosine component of the secondary fluctuation, respectively. Noted that the superscript m represents the symbol +, − and n represent the symbols *d* and *q*.

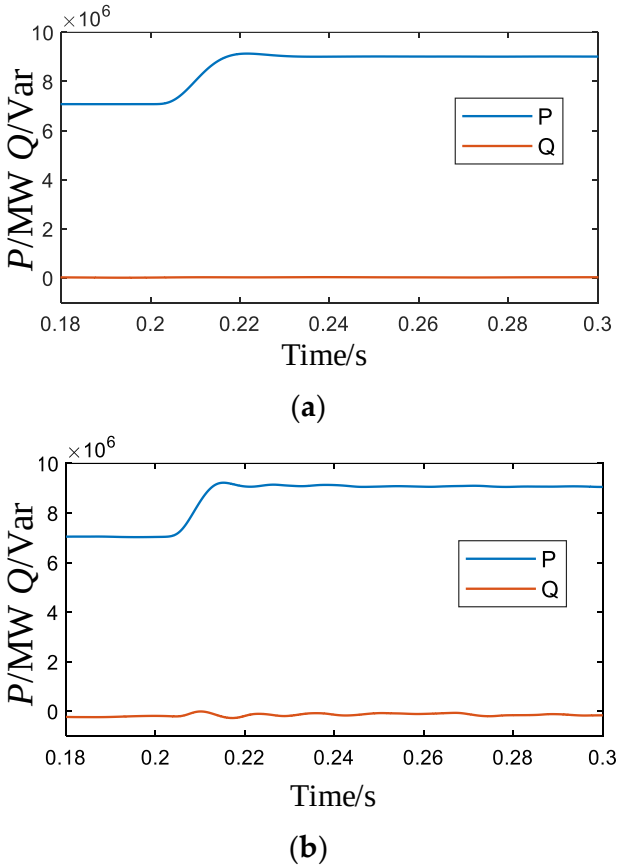

Figure 14. Waveforms of active and reactive power under active power changes: (**a**) RBFSMC; (**b**) PI control.

Table 5. Simulation result analysis of power.

Power		Maximum Power	Dynamic Response Time
RBFSMC	Active power	9.098 MW	20 ms
	Reactive power	0 Var	0 s
PI control	Active power	9.2 MW	35 ms
	Reactive power	0.14 MVar	30 ms

When the grid voltage is unbalanced, the grid-side current will fluctuate. Therefore, the reference current should be changed according to Equation (28)

$$\begin{cases} i_{d\ \mathrm{ref}}^{+} = \frac{2}{3}\frac{u_{sq}^{+}P_{s0}+u_{sd}^{+}Q_{s0}}{\left(u_{sd}^{+}\right)^{2}+\left(u_{sq}^{+}\right)^{2}} \\ i_{q_{\mathrm{ref}}}^{+} = \frac{2}{3}\frac{u_{sq}^{+}P_{s0}+u_{sd}^{+}Q_{s0}}{\left(u_{sd}^{+}\right)^{2}+\left(u_{sq}^{+}\right)^{2}} \end{cases} \tag{29}$$

Figure 15 shows the waveforms of the grid-side current under unbalanced grid voltage, respectively. Simulation result analysis of grid-side current under unbalanced voltage is shown in Table 6. As can be seen from Figure 15, the current unbalance factor (CUF) of three-phase grid current under RBFSMC control is 0.8%, while the CUF under PI control is 1.7%. The peak current under RBFSMC is 405 A, while the peak current under PI control is 454 A. Therefore, RBFSMC is better than PI control.

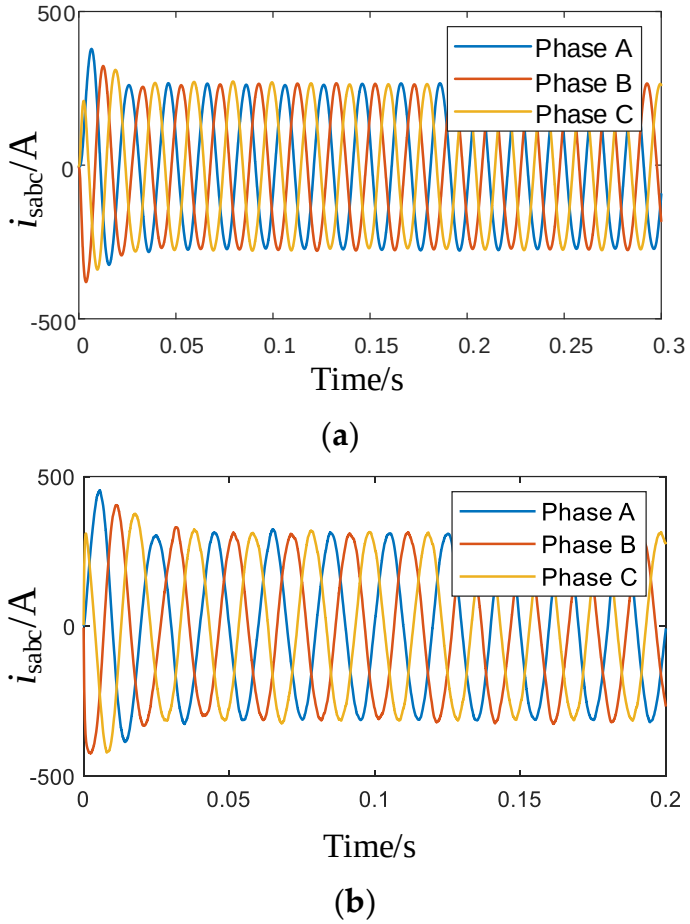

Figure 15. Waveforms of grid-side current under unbalanced voltage control: (**a**) RBFSMC; (**b**) PI control.

Table 6. Simulation result analysis of grid-side current.

Grid-Side Current	CUF	FFT	Maximum Inrush Current
RBFSMC	0.8%	1.4%	405 A
PI control	1.7%	1.93%	454 A

Figure 16 shows the waveforms of power under unbalanced grid voltage, respectively. Simulation result analysis of power is shown in Table 7. The maximum active power is 10.7 MW while it is 12.7 MW under PI control. The active power fluctuation is less than PI control. Reactive power fluctuations under PI control are also more frequent.

Table 7. Simulation result analysis of power.

Power		Maximum Power	Dynamic Response Time
RBFSMC	Active power	10.7 MW	30 ms
	Reactive power	0.05 MVar	22 ms
PI control	Active power	12.7 MW	36 ms
	Reactive power	0.2 MVar	33 ms

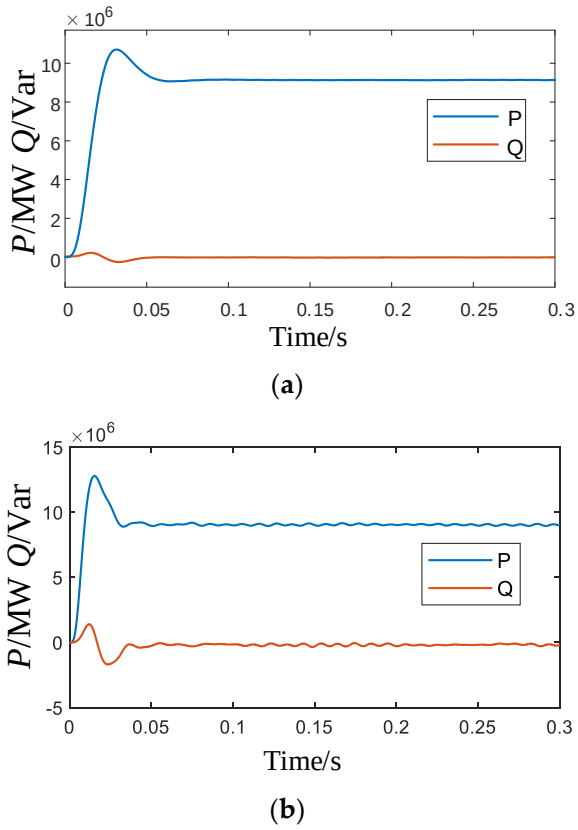

Figure 16. Waveforms of active and reactive power under unbalanced grid voltage: (**a**) RBFSMC; (**b**) PI control.

6. Experiment Results

In order to verify the effectiveness of the proposed RBFSMC, the hardware-in-the-loop experiment was built on the RT-LAB OP5700 platform. The controller uses DSP TMS32F28335 made by TI company, and the output waveform from RT-LAB is viewed by an oscilloscope and host. The RT-LAB OP5700 platform is shown in Figure 17.

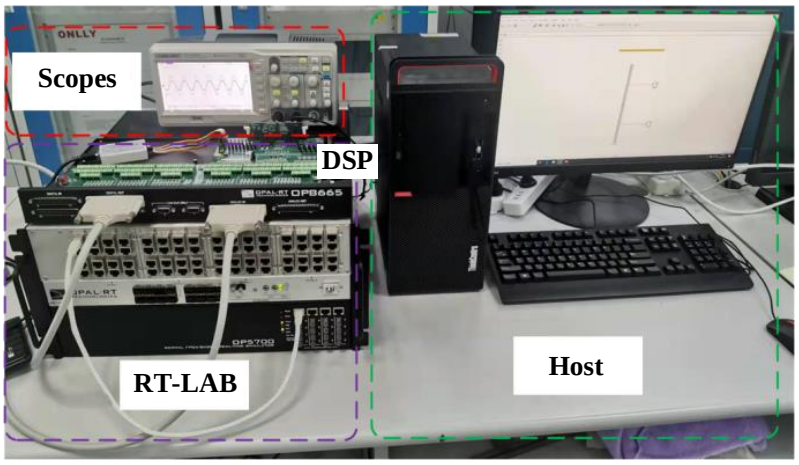

Figure 17. Hardware in the loop simulation experiment platform.

In this paper, RT-LAB is used to simulate the topology shown in Figure 1. The RBFSMC proposed in this paper is implemented on the DSP. When the RT-LAB is running, the current and voltage signals will be passed to the DSP, and the DSP will generate PWM signals to

the RT-LAB after calculation to form a closed loop. In this experiment, the DSP sampling frequency was set to 1 MHz. Experimental parameters were consistent with the simulation.

Figure 18 shows grid voltages and line currents of MMC. The grid current signals are sinusoidal and have no phase difference with the grid voltage. When the active power setting value increases, the amplitude of grid current will also change. However, there is no ripple while the setting value changes like the simulation. These results confirm that the RBFSMC can operate well in MMC.

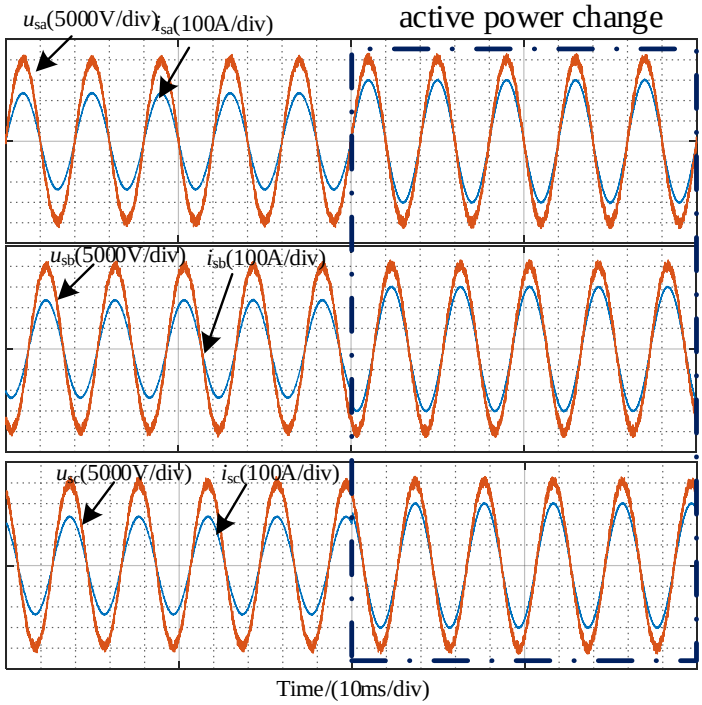

Figure 18. Grid voltages and line currents (u_{sa},i_{sa}), (u_{sb},i_{sb}), and (u_{sc},i_{sc}).

Figure 19 shows grid-side active and reactive power of MMC. When the active power setting value increases from 7 to 9 MW, the reactive power does not fluctuate. The active power reached stability after 20 ms. Therefore, when the reference value changes it does not change the fact that the power factor is the unit.

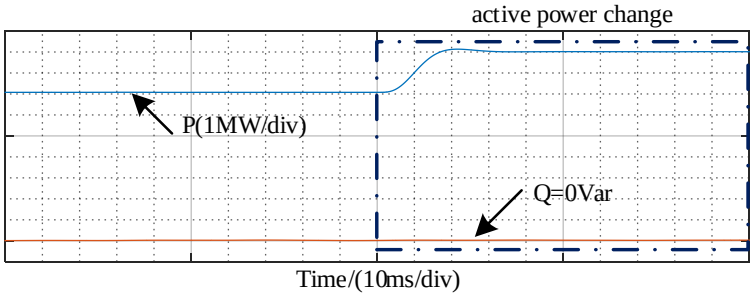

Figure 19. Grid-side active and reactive power.

7. Conclusions

A new approach to the implementation of sliding mode controller based on RBF design was proposed in this paper. As such, the benefits of sliding mode control and RBF can be combined. In this sense, the controller parameter problems were explicitly dealt with, and the system robustness performance could be enhanced. Compared with the conventional SMC strategies, the novelty of the proposed methodology was that it did not require precise mathematical models and can identify the system dynamics, facilitate the

successful suppression of performance deterioration caused by parameter variations and model inaccuracy. Finally, the simulation verification shows that the proposed RBFSMC for MMC can be assessed by steady-state and dynamic performance.

Author Contributions: X.Y. established the original conception, provided the technical guidance and checked the data. H.F. modeled the system, designed the algorithms of control strategy and wrote the paper. All authors have read and agreed to the published version of the manuscript.

Funding: This work was supported by National Science Foundation of China (51777120) and Shanghai 2021 "Science and Technology Innovation Action Plan" Science and Technology Support for Carbon Neutralization (the first batch) (21DZ1207502).

Institutional Review Board Statement: Not applicable.

Informed Consent Statement: Not applicable.

Conflicts of Interest: The authors declare that they have no known competing financial interests or personal relationships that could have appeared to influence the work reported in this paper.

Abbreviations

MMC	Modular multilevel converter;
CUF	Current unbalance factor;
PI	Proportional-integral controller;
PR	Proportional resonant;
MPC	Model predictive control;
NN	Neural network;
THD	Total Harmonic Distortion;
RBF	Radial basis function;
RBFNN	RBF neural network;
RBFSMC	RBF neural network-based sliding mode control;
SM	Sub-modules;
FFT	Fast Fourier transforms.

References

1. Debnath, S.; Qin, J.; Bahrani, B.; Saeedifard, M.; Barbosa, P. Operation, Control, and Applications of the Modular Multilevel Converter: A Review. *IEEE Trans. Power Electron.* **2015**, *30*, 37–53. [CrossRef]
2. Perez, M.A.; Bernet, S.; Rodriguez, J.; Kouro, S.; Lizana, R. Circuit Topologies, Modeling, Control Schemes, and Applications of Modular Multilevel Converters. *IEEE Trans. Power Electron.* **2014**, *30*, 4–17. [CrossRef]
3. Allebrod, S.; Hamerski, R.; Marquardt, R. New Transformerless, Scalable Modular Multilevel Converters for HVDC-Transmission. In Proceedings of the 2008 IEEE Power Electronics Specialists Conference, Rhodes, Greece, 15–19 June 2008; pp. 174–179. [CrossRef]
4. Mehrasa, M.; Pouresmaeil, E.; Zabihi, S.; Catalao, J.P.S. Dynamic model, control and stability analysis of MMC in HVDC transmission systems. *IEEE Trans. Power Deliv.* **2017**, *32*, 1471–1482. [CrossRef]
5. Moon, J.W.; Park, J.W.; Kang, D.W.; Kim, J.M. A Control Method of HVDC-Modular Multilevel Converter Based on Arm Current Under the Unbalanced Voltage Condition. *IEEE Trans. Power Deliv.* **2015**, *30*, 529–536. [CrossRef]
6. Li, S.; Wang, X.; Yao, Z.; Li, T.; Peng, Z. Circulating Current Suppressing Strategy for MMC-HVDC Based on Nonideal Proportional Resonant Controllers Under Unbalanced Grid Conditions. *IEEE Trans. Power Electron.* **2015**, *30*, 387–397. [CrossRef]
7. Yang, Q.; Saeedifard, M.; Perez, M.A. Sliding Mode Control of the Modular Multilevel Converter. *IEEE Trans. Ind. Electron.* **2019**, *66*, 887–897. [CrossRef]
8. Bergna, G.; Garces, A.; Berne, E.; Egrot, P. A generalized power control approach in ABC frame for modular multilevel converters based on Lagrange multipliers. *IEEE Trans. Power Deliv.* **2014**, *29*, 386–394. [CrossRef]
9. Barnklau, H.; Gensior, A.; Rudolph, J. A Model-Based Control Scheme for Modular Multilevel Converters. *IEEE Trans. Ind. Electron.* **2013**, *60*, 5359–5375. [CrossRef]
10. Antonopoulos, A.; Angquist, L.; Harnefors, L.; Ilves, K.; Nee, H.P. Global Asymptotic Stability of Modular Multilevel Converters. *IEEE Trans. Ind. Electron.* **2013**, *61*, 603–612. [CrossRef]
11. Yang, S.; Peng, W.; Yi, T. Feedback Linearization-Based Current Control Strategy for Modular Multilevel Converters. *IEEE Trans. Power Electron.* **2017**, *33*, 161–174. [CrossRef]
12. Gong, Z.; Wu, X.; Dai, P.; Zhu, R. Modulated Model Predictive Control for MMC-Based Active Front-End Rectifiers Under Unbalanced Grid Conditions. *IEEE Trans. Ind. Electron.* **2019**, *66*, 2398–2409. [CrossRef]

13. Guan, W.; Huang, S.; Luo, D.; Rong, F. A Reverse Model Predictive Control Strategy for a Modular Multilevel Converter. *Energies* **2019**, *12*, 297. [CrossRef]
14. Zhi, W.; Chu, J.; Wei, G.; Huang, Q.; Chen, L.; Yuan, X. Hybrid Modulated Model Predictive Control in a Modular Multilevel Converter for Multi-Terminal Direct Current Systems. *Energies* **2018**, *11*, 1861.
15. Fei, J.; Wang, H.; Fang, Y. Novel Neural Network Fractional-Order Sliding-Mode Control With Application to Active Power Filter. *IEEE Trans. Syst. Man Cybern. Syst.* **2021**, 1–11. [CrossRef]
16. Novak, M.; Dragicevic, T. Supervised imitation learning of finite set model predictive control systems for power electronics. *IEEE Trans. Ind. Electron.* **2020**, *29*, 1717–1723. [CrossRef]
17. Wang, S.; Dragicevic, T.; Gao, Y.; Teodorescu, R. Neural Network based Model Predictive Controllers for Modular Multilevel Converters. *IEEE Trans. Energy Convers.* **2020**, *36*, 1562–1571. [CrossRef]
18. Liu, X.; Qiu, L.; Wu, W.; Ma, J.; Wang, D. Predictor-Based Neural Network Finite Set Predictive Control for MMC. *IEEE Trans. Ind. Electron.* **2020**, *68*, 11621–11627. [CrossRef]
19. Mohamed, I.S.; Rovetta, S.; Do, T.D.; Dragicevic, T.; Diab, A. A Neural-Network-Based Model Predictive Control of Three-Phase Inverter With an Output LC Filter. *IEEE Access* **2019**, *7*, 124737–124749. [CrossRef]
20. Ostrowsky, G.M. Application of nonlinear corrective devices in second order automatic control systems. *Avtomat I Telemeh* **1956**, *17*, 979–984.
21. Utkin, V. Variable structure systems with sliding modes. *IEEE Trans. Autom. Control* **2003**, *22*, 212–222. [CrossRef]
22. Mazumder, S.K.; Nayfeh, A.H.; Borojevic, A. Robust Control of Parallel DC-DC Buck Converters by Combining Integral-Variable-Structure and Multiple-Sliding-Surface Control Schemes. *IEEE Trans. Power Electron.* **2002**, *17*, 428–437. [CrossRef]
23. Mazumder, S.K.; Kamisetty, S.L. Design and experimental validation of a multiphase VRM controller. *IEE Proc. Electr. Power Appl.* **2005**, *152*, 1076–1084. [CrossRef]
24. Tan, S.C.; Lai, Y.M.; Tse, C.K. A unified approach to the design of PWM-based sliding-mode voltage controllers for basic DC-DC converters in continuous conduction mode. *IEEE Trans. Circuits Syst. I Regul. Pap.* **2006**, *53*, 1816–1827.
25. Fridman, L.; Spurgeon, S.K. *Variable Structure Systems: From Principles to Implementation*; IET: London, UK, 2004.
26. Xu, Z.B.; Min, J.Q.; Jian, R. Adaptive Neuro Sliding Mode Control of Nonlinear System. In Proceedings of the 2008 International Conference on Intelligent Computation Technology and Automation (ICICTA), Changsha, China, 20–22 October 2008.
27. Wang, R.; Zhao, Y.; Miao, K. Application of Neural Network Minimum Parameter Learning Algorithm in Ship's Heading Tracking Control. In Proceedings of the 2016 9th International Symposium on Computational Intelligence and Design (ISCID), Hangzhou, China, 10–11 December 2016.
28. Wang, Y.; Qi, L.; Wang, X.G.; Liu, J. Simulation experiment of flexible parallel robot control by RBF neural network based on sliding mode robust term. In Proceedings of the 2017 2nd Asia-Pacific Conference on Intelligent Robot Systems (ACIRS), Wuhan, China, 16–18 June 2017.
29. Zhou, Z.; Tang, G.; Huang, H.; Yuan, Z. Adaptive Neural Disturbance Observer Based Nonsingular Fast Terminal Sliding Mode Control for Underwater Robot Manipulators. In Proceedings of the 2019 International Conference on Control, Automation and Information Sciences (ICCAIS), Chengdu, China, 23–26 October 2019.
30. Wang, Z.; Li, Y.; Gao, S.; Meng, L.; Ran, T. RBF Neural Network Sliding Mode control for Aeronautical Remote Sensing Stable Platform. In Proceedings of the 2020 Chinese Automation Congress (CAC), Shanghai, China, 6–8 November 2020.